

Three-dimensional nano-optical assembly of antenna structures with collective near-field coupling

Mamoru Tamura^{1,2} · Takuya Iida¹

Received: 2 July 2015 / Accepted: 18 September 2015 / Published online: 22 October 2015
© Springer-Verlag Berlin Heidelberg 2015

Abstract Metallic nanostructures are used for various applications because of their characteristic optical responses that generate strong near-fields. We have theoretically clarified that the configuration of nanoparticles (NPs) and their optical properties can be controlled by optical manipulation. In this study, we greatly improved our previously reported simulation method, and this improvement enables investigation of the stable states of optically trapped NPs in a three-dimensional system. On the basis of this method, the assembly process of rod-shaped silver NPs is concisely clarified, where NPs of a specific shape are selectively assembled even in a mixture of NPs of different shapes. In particular, our simulation method clarifies how a light-induced force drives assembly processes, which is an important subject to consider for extending the degree of freedom of an optical manipulation. Furthermore, as reported in our previous studies, an assembled structure inherits the properties of light used for the optical trapping; e.g., rod-shaped silver NPs are radially connected to each other and assembled into a ring-shaped structure under the irradiation of a radially polarized vector beam with a ring-shaped intensity distribution. The assembled structure is an artificial light-harvesting antenna because it theoretically exhibits an enhancement of near-field and extinction in a

broader wavelength range than that of the original NPs composing the antenna and also a response to the non-polarized light such as the sunlight. On the basis of an optically manipulated configuration of NPs and their optical properties, we discuss the selective optical assembly in a three-dimensional simulation.

1 Introduction

Metallic nanostructures have the characteristic optical properties of enhancement of near-field, scattering, and absorption because of the collective oscillation of electrons. They have attracted the interest of many researchers because of their potential for a wide range of applications, for example metamaterials realizing an optically negative index [1, 2] and metallic photonic crystals for visible light sources [3]. Lithography and etching are two methods of constructing such structures with high accuracy [4–6]. In contrast, a bottom-up process based on self-assembly enables an orderly arrangement of nanoparticles (NPs) [7–9]. Synthesis methods for NPs of various shapes such as rod-, cage-, and star-shaped NPs have been studied [10–12], and therefore, how to arrange these NPs is an important subject to study for effectively improving the optical properties based on the interaction between NPs.

We have previously clarified the possibility of controlling the optical properties of metallic NPs via optical manipulation of their alignment [13]. Characteristic light such as the Laguerre–Gaussian beam with angular momentum and holographic laser with arbitrary light intensity can be generated to realize a variety of optical manipulations of small objects. By using a vector beam with a ring-shaped intensity distribution and axially symmetric polarization, we have theoretically and

✉ Mamoru Tamura
m-tamura@pe.osakafu-u.ac.jp

✉ Takuya Iida
t-iida@p.s.osakafu-u.ac.jp

¹ Department of Physical Science, Graduate School of Science, Osaka Prefecture University, Osaka 599-8531, Japan

² Department of Physics and Electronics, Graduate School of Engineering, Osaka Prefecture University, Osaka 599-8531, Japan

experimentally demonstrated that silver NPs are assembled on a substrate according to the properties of incident light [14, 15]. In particular, even in a dispersion liquid including NPs of various shapes, the NPs of a specific shape are selectively assembled and a two-dimensionally isotropic optical antenna with the property of harvesting broadband light is constructed.

Nanostructures exhibiting any desired optical properties can be constructed by optical manipulation, and the range of their potential application can be expanded by the development of laser and manipulation techniques. Against this background, establishing a method for predicting the configuration of assembled structures under arbitrary light and their optical properties is necessary. In particular, clarifying how the light-induced force (LIF) drives the assembly process is important.

Therefore, in this study, we greatly improved our previously developed simulation method, the Light-induced-force Nano-Metropolis Method (LNMM), to simultaneously investigate the configuration of assembled structures and their assembly process under irradiation. As the assembly target, we assumed rod-shaped silver NPs under a radially polarized vector beam with a ring-like intensity distribution. In our previous research, NPs of a specific shape were selectively assembled from a mixture of NPs of various shapes. When considering such a selectivity, how the LIF affects the NPs is important to understand, but LIF is very complex because of the interaction between NPs. Our improved LNMM clarifies how the LIF acts and the selective assembly process of NPs. Furthermore, the assembled structures show a characteristic optical response based on their configuration, which is controlled by the vector beam. We also discuss the optical properties of assembled structures that can be treated as artificial light-harvesting antennae.

2 Calculation methods

2.1 Light-induced-force nano-Metropolis method

To investigate the stable states of NPs under irradiation, we have previously developed the LNMM on the basis of the Metropolis method and a general expression of LIF [16] derived from the Lorentz force. The general expression of time-averaged LIF is

$$\mathbf{F}_{\text{LIF}} = \frac{1}{2} \text{Re} \left[\sum_{\omega} \int_V d\mathbf{r} (\nabla \mathbf{E}(\mathbf{r}, \omega)^*) \cdot \mathbf{P}(\mathbf{r}, \omega) \right] \quad (1)$$

where \mathbf{E} is the response field, \mathbf{P} is the induced polarization, ω indicates the angular frequencies for irradiation of any lasers, and V indicates the region where the NP exists. To operate the volume integral, NPs are approximately divided

into any number of spherical cells, with each cell assigned to a sequential index. When the wavelength of incident light is sufficiently longer than the size of a cell, the LIF acting on the i -th cell becomes $\mathbf{F}_i = \frac{1}{2} \text{Re} [(\nabla \mathbf{E}_i^*) \cdot \mathbf{P}_i V_i]$, where \mathbf{E}_i and \mathbf{P}_i are homogeneous in the region of the i -th cell with the volume V_i under the long wavelength approximation. \mathbf{E}_i and \mathbf{P}_i are given by self-consistently solving the following simultaneous equations:

$$\mathbf{E}_i = \mathbf{E}^{(0)}(\mathbf{r}_i) + \sum_{j \neq i}^N \mathbf{G}(\mathbf{r}_i - \mathbf{r}_j) \mathbf{P}_j V_j + \mathbf{S}_i \mathbf{P}_i \quad (2)$$

$$\mathbf{P}_i = \chi_i \mathbf{E}_i \quad (3)$$

where \mathbf{r}_i is the center position of the i -th cell, $\mathbf{E}^{(0)}$ is the electric field of incident light, N is the number of cells, \mathbf{G} is the Green's function in a homogeneous medium, $\mathbf{S}_i = \int_{V_i} d\mathbf{r}' \mathbf{G}(\mathbf{r}_i - \mathbf{r}')$ is the analytical integral result for $j = i$, and χ_i is the electric susceptibility given by the Drude model in a visible light region.

The stable states of NPs during their random motion can be investigated by the Metropolis method, in other words, a Monte Carlo method, based on the balance between the thermal fluctuations and the potential profile due to the LIF. In the Metropolis method, the motion of NPs in each step is carried out according to the following probability:

$$p = \begin{cases} 1, & (\Delta H \leq 0) \\ \exp(-\Delta H/k_B T), & (\Delta H > 0) \end{cases} \quad (4)$$

where k_B is the Boltzmann constant, T is the temperature of medium, and ΔH is the change in the potential of the total system between before and after the motion of NPs. In each step, we assume that the random motion of individual NPs is attempted in order (simultaneous movement of all NPs is also possible). When a NP is translationally displaced by $\Delta \mathbf{r}$ and rotated by $\Delta \boldsymbol{\theta}$, ΔH is evaluated as follows:

$$\Delta H = -\mathbf{F}_{\text{NP}} \cdot \Delta \mathbf{r} - \boldsymbol{\tau}_{\text{NP}} \cdot \Delta \boldsymbol{\theta} + \Delta V_{\text{DLVO}} \quad (5)$$

where the magnitude of displacement and the change in LIF between before and after the motion must be sufficiently small. The LIF and torque acting on the NP are given by $\mathbf{F}_{\text{NP}} = \sum_i \mathbf{F}_i$ and $\boldsymbol{\tau}_{\text{NP}} = \sum_i \mathbf{d}_i \times \mathbf{F}_i$, respectively, where the sum is operated for the cells composing the NP and \mathbf{d}_i is the distance between the rotation axis and each cell. However, focusing on $\Delta \mathbf{r}_i^{\text{rot}}$, which is the displacement of each cell by the rotation, the rotation potential change is given by $\boldsymbol{\tau}_{\text{NP}} \cdot \Delta \boldsymbol{\theta} = \sum_i (\Delta \boldsymbol{\theta} \times \mathbf{d}_i) \cdot \mathbf{F}_i = \sum_i \Delta \mathbf{r}_i^{\text{rot}} \cdot \mathbf{F}_i$. Therefore, Eq. (5) is rewritten as

$$\Delta H = -\sum_i \mathbf{F}_i \cdot \Delta \mathbf{r}_i + \Delta V_{\text{DLVO}} \quad (6)$$

where $\Delta \mathbf{r}_i = \Delta \mathbf{r} + \Delta \mathbf{r}_i^{\text{rot}}$. However, when NP motion is attempted, the translational and rotational motions can be

attempted separately. Then, the last term on the right-hand side of Eq. (6) evaluates the phenomenological attractive and repulsive forces due to the van der Waals force and electric double layer based on the DLVO theory. To calculate the DLVO interaction between rod-shaped NPs, we substitute the expression for the spherical particles [17]. The rod-shaped NPs are divided into any number of spherical cells, similar to the LIF calculation, and the diameter of the cells corresponds to the length of the short axis of the NPs. ΔV_{DLVO} is obtained by evaluating the DLVO potential between all cells and its difference between before and after the motion of NPs. After the potential change is calculated, all motions are not always accepted and carried out according to the probability of Eq. (4). By repeating this procedure 10^6 times, we can finally obtain the assembled configuration of NPs as the stable state.

To perform the simulation of assembly, we must record not only the position but also the orientation of NPs for non-spherical objects. In the case where only in-plane rotation in a two-dimensional system is considered, it is sufficient to record the rotation angle from the axis perpendicular to the system. Therefore, also for three rotational degrees of freedom in a three-dimensional system, Euler angles, which express the rotation around the each coordinate axis, can be easily employed. However, using Euler angles is not suitable because they cause the gimbal-lock problem, which reduces the rotational degrees of freedom. Instead, using the quaternions, which can express the orientation by the rotation around an arbitrary axis, is a widely employed method. The quaternions have scalar and vector components; for example, the quaternion expressing a θ rotation around the unit vector \mathbf{v} is $q = (\cos \theta/2, \mathbf{v} \sin \theta/2)$. Then, the vector \mathbf{r}' after the rotation of \mathbf{r} by q is expressed as $\mathbf{r}' = q\mathbf{r}q^*$, where q^* is the conjugate of q and the product is operated along the rules of quaternion. Additionally, further rotation q' after q is expressed by $q'q$. Thus, we can simply perform the simulation with three-dimensional rotation.

2.2 Calculation model

The detailed calculation model is shown in Fig. 1. The substrate exists at $z > 0$, whereas at $z < 0$, there is room-temperature water where NPs can move. Two types of rod-shaped silver NPs with approximately equal volume but different length are assumed as the NPs; long and short NPs are indicated by red and blue color, respectively, in Fig. 1a. To calculate the LIF acting on the anisotropic NPs, the long and short NPs are expressed by three- and two-connected spheres as the cells, respectively. In the initial state, NPs are configured in a grid at $z = -1 \mu\text{m}$, and

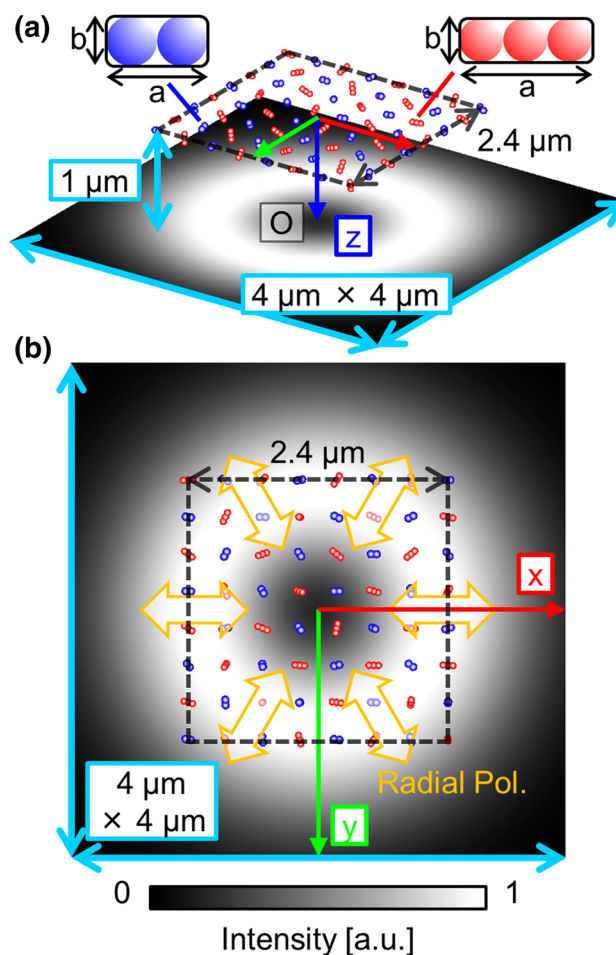


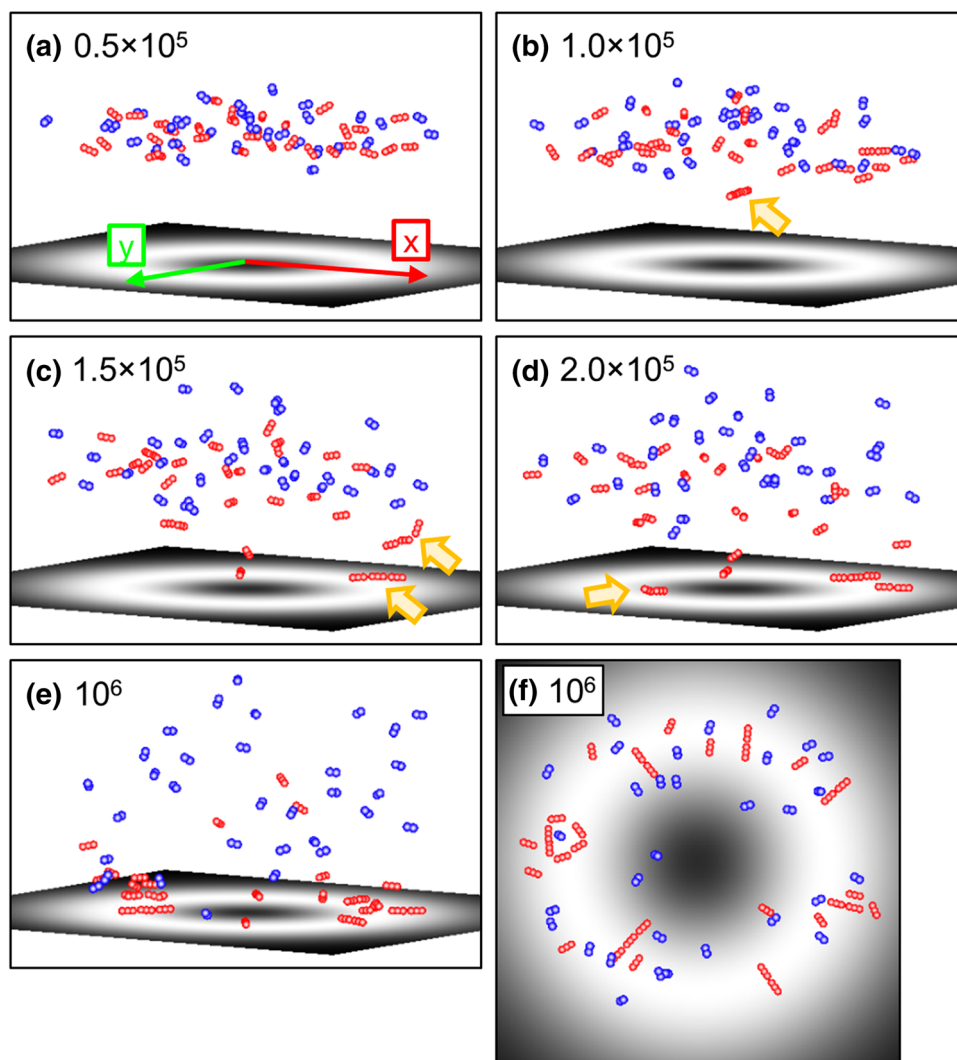
Fig. 1 Calculation model of LNMM. The intensity distribution on the substrate and the initial configuration of NPs are shown in **a** three-dimensional and **b** top-side (x - y) views. The symbols a and b in **a** show the length of long and short axes of NPs, respectively, $a = 120 \text{ nm}$ and $b = 40 \text{ nm}$ for long NPs, $a = 91.56 \text{ nm}$ and $b = 45.78 \text{ nm}$ for short NPs. The divided spheres in NPs correspond to the cells in the calculation of the DLVO potential. The cells in the calculation of the LIF are also similar, but they have a slightly larger size to compensate for the volume of the original NPs

orientated randomly. As the incident light $\mathbf{E}^{(0)}$, we assume a z -propagating radially polarized vector beam whose focal point exists at the origin; its power is 50 mW, and the radius of the highest intensity contour, as the spot size, is $1 \mu\text{m}$. In each step of the simulation, random translational displacement within 1 nm and random rotation around a random direction within 1° are employed as $\Delta \mathbf{r}$ and $\Delta \theta$, respectively.

2.3 Calculation of optical response

After the optically assembled structures under the radial vector beam are obtained by the LNMM simulation, we evaluate their optical response by using the plane waves as

Fig. 2 **a–e** Snapshots of each step in LNMM simulation. **f** *Top* (*x–y*) view of **e**, which is the final configuration



another incident light $\mathbf{E}^{(0)}$. The LIF for a plane wave does not include the gradient force; therefore, the z -component of LIF under the z -propagating plane wave is proportional to the extinction as a sum of absorption and scattering:

$$\langle \sigma_{\text{ext}} \rangle \propto \left| \sum_i F_{i,z} \right|, \quad (7)$$

where the momentum conservation law is satisfied. Therefore, we can understand how the optically assembled structures respond to the white light by calculating the LIF when the plane wave is used as the incident light $\mathbf{E}^{(0)}$.

3 Results and discussion

Figure 2 shows the process whereby NPs are moved and converged to the stable states. This process appears as a time-dependent assembly process, but the steps in the process do not indicate the time-dependent dynamics of

NPs. In each step, NPs are randomly displaced according to the probability of Eq. (4). However, the LIF acting on the NPs can be obtained during the LNMM simulation; therefore, the timescale of simulation can be estimated via the diffusion speed and friction coefficient of NPs in the medium. Additionally, strict time dependence is obtained by simulation based on the Langevin equation. Previously, we have also reported such time-dependent simulation studies [13, 18], and we can discuss the correspondence relationship. On the other hand, the qualitative assembly process driven by LIF can be understood from Fig. 2. If the NPs are acted on by stronger forces, they move and converge to stable states in fewer steps. Based on this concept, we can confirm that the forces acting on the long NPs are clearly stronger than those acting on the short NPs.

As shown in Fig. 3a, b, in the visible light region, the silver NPs have a strong optical response caused by the localized surface plasmon resonance (LSPR). The short axis LSPR peaks of both NPs exist at almost the same

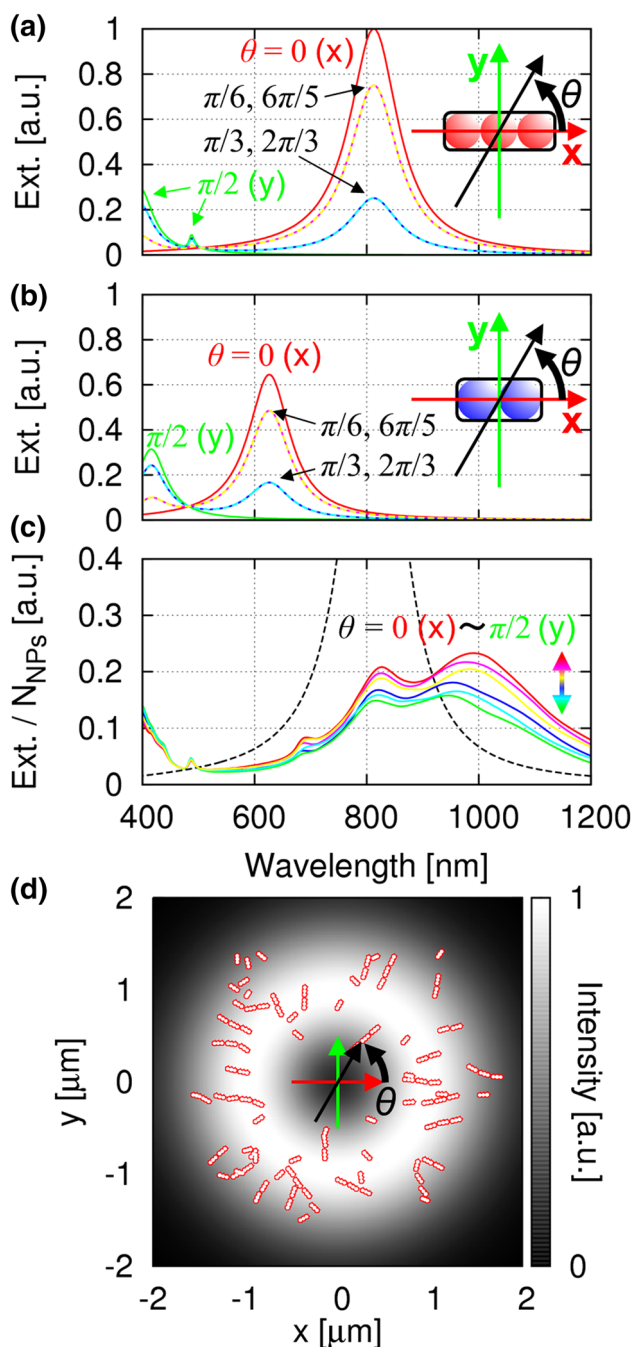


Fig. 3 Extinction spectra of **a** the long NP, **b** short NP, and **c** assembled structure **d** obtained by LNMM simulation for 100 long NPs. Spectra are evaluated by the z -propagating plane wave with a specific polarization direction ($\theta = 0, \pi/6, \pi/3, \pi/2, 2\pi/3, 5\pi/6$) and normalized by the maximum value of long NP $\theta = 0(x)$ and the number of NPs

wavelength near 400 nm, whereas the long axis LSPR peaks exist near 630 nm for the short NPs and 810 nm for the long NPs. The wavelength of light used for the assembly is 1064 nm, which is different from both of the long axis LSPR peaks, but the long NPs can be assembled on the substrate because the LSPR peaks have a long tail.

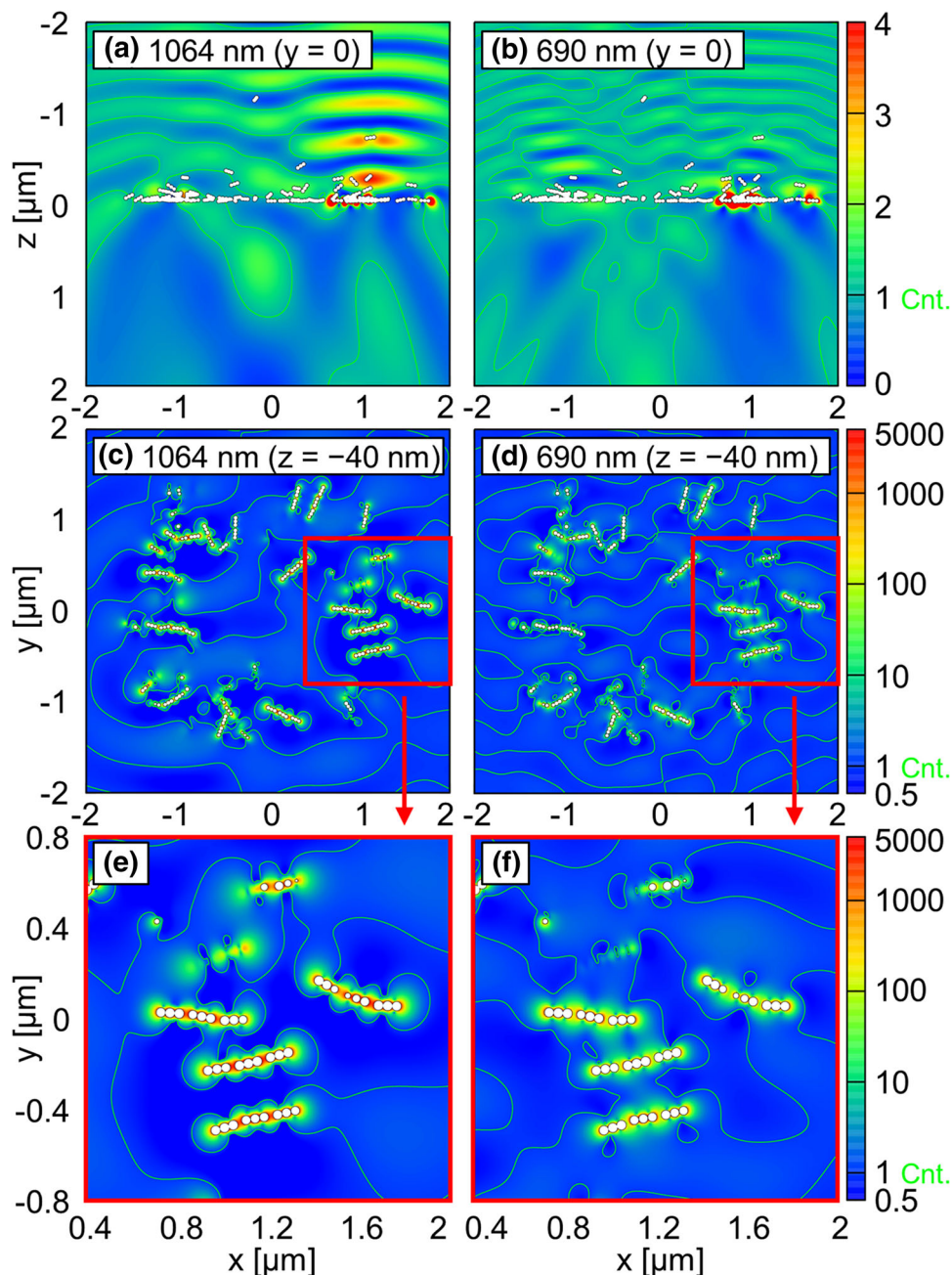
The short NPs are also pushed weakly by the LIF; therefore, their average z -position can approach $z = 0$, but individual NPs undergo Brownian motion because of thermal fluctuations, and these are not assembled. Therefore, by employing the LNMM, the reason why NPs of a specific shape are selectively assembled in a system including NPs of various shapes can be understood.

The motion of long NPs shows another interesting phenomenon. The NPs indicated by the orange arrows in Fig. 2 can be understood as being pushed by a very strong LIF because they reach the substrate in a small number of steps, and in particular, they are connected in the longitudinal direction of NPs. These connections induce the collective mode of longitudinal LSPR of long NPs and make the LSPR peak wavelength red-shifted and closer to the incident light wavelength of 1064 nm. Therefore, connected NPs with a resonant wavelength near 1064 nm are pushed by a strong LIF, and the structures that can effectively respond to the incident light are selectively assembled. Additionally, Fig. 2f shows that the assembled structures are dependent on the intensity distribution and polarization direction of the incident light. This result means that the assembled structures inherit the properties of incident light such as the wavelength and the profile of electric fields.

We now focus on the optical properties of the assembled structure, which can be expected to be modulated by the incident light. To emphasize the characteristics, we perform the LNMM simulation for 100 long NPs. In the initial state, they are located in a square region of $2.4 \times 2.4 \mu\text{m}^2$, similar to Fig. 1a. The assembled structure obtained by LNMM is shown in Fig. 3d, and its extinction spectra under the plane wave with polarization in various directions are shown in Fig. 3c. In addition to the original LSPR peak of long NPs, we can confirm two different peaks near the wavelengths 1064 and 690 nm. As mentioned previously, both these peaks are attributed to the collective mode of longitudinal LSPR. Here, 1064 and 690 nm represent bonding and anti-bonding modes because their peak energies are decreased and increased by the attractive and repulsive interactions, respectively. The appearance of such modes makes the total spectra very broadened. Furthermore, the extinction spectra have less dependence on the polarization direction because the structure is assembled according to the axially symmetric intensity distribution and polarization direction. Therefore, even under the non-polarized white light, the assembled structure can effectively respond to the light differently from the initial condition.

Additionally, Fig. 4 shows the response field for both 1064 and 690 nm. As shown in a, b, the x -polarized plane wave propagates in the z -direction and is reflected by the assembled structures at both wavelengths. In particular, in the region near $x = 1 \mu\text{m}$, the light of (a) 1064-nm

Fig. 4 Enhancement degree of response field for the assembled structure of Fig. 3d under the irradiation of x -polarized plane wave corresponding to Fig. 3c. **a, b** and **c–f** are x - z and x - y distributions, respectively. As the wavelength, **a, c, e** 1064 nm for the bonding mode and **b, d, f** 690 nm for the anti-bonding mode are assumed. **c–f** is the cross section at $z = -40$ nm, because the NPs are not perfectly attached to the substrate. **e** and **f** show enlarged views of the areas enclosed by the red lines in **c** and **d**. The green lines in the figure show the contour lines indicating 1. In **a, b**, the projections of all NPs are shown by the white regions, whereas in **c–f**, the cross sections at $z = -40$ nm are shown



wavelength is strongly reflected because there are densely assembled NPs and LSPR is redshifted, as shown in the area enclosed by the red line of (c). In contrast, for (b) 690 nm, the reflection is not strong, and therefore, there is a possibility to realize wavelength-selective reflection if an appropriate wavelength is chosen to assemble the structures. Furthermore, focusing on the near-field enhanced near the assembled NPs in c–f, we can confirm that an enhancement factor of more than a thousand is obtained. Such an enhancement due to the collective modes can be induced for a wide range of wavelengths according to Fig. 3c. Therefore, the assembled NPs play a role of optical antenna and show promise for

application in various research fields. For example, wavelength-selective reflection can be used for the mirrors to improve solar devices [19], and near-field enhancement for a wide range of wavelengths can be used for surface-enhanced Raman scattering [20].

4 Conclusion

We have improved our developed simulation method LNMM, which enables investigation of the stable configuration of NPs of various shapes under the irradiation of

arbitrary light. By using LNMM, we have theoretically clarified the assembly process where the longitudinally connected long NPs are acted on by a particularly strong LIF and selectively assembled on the substrate. Under the irradiation of a radially polarized vector beam with a ring-like intensity distribution, a ring-like structure of NPs is assembled and radially aligned. As an artificial antenna, the assembled structure shows the characteristic properties of broadband near-field enhancement and extinction and wavelength-selective reflection. These structures have potential for the use in various applications such as solar devices and surface-enhanced Raman scattering. The results obtained in this study significantly extend the degree of freedom in constructing and controlling a variety of optically assembled structures and their optical properties.

Acknowledgments The authors thank Prof. S. Ito and Prof. S. Tokonami for their helpful discussions from the experimental viewpoints. We also thank Prof. H. Ishihara for his encouragement and support. This work was supported in part by a Grant-in-Aid for JSPS Fellows (No. 14J08760), a Grant-in-Aid for Scientific Research (B) No. 26286029 from the JSPS, and Grants-in-Aid for Exploratory Research No. 26610089 from JSPS, JST-SENTAN, the Nakatani Foundation, and the Canon Foundation.

References

1. N. Engheta, Circuits with light at nanoscales: optical nanocircuits inspired by metamaterials. *Science* **317**, 1698–1702 (2007)
2. A. Boltasseva, V.M. Shalaev, Fabrication of optical negative-index metamaterials: recent advances and outlook. *Metamaterials* **2**, 1–17 (2008)
3. S. Belousov, M. Bogdanova, A. Deinega, S. Eyderman, I. Valuev, Y. Lozovik, I. Polischuk, B. Potapkin, B. Ramamurthi, T. Deng, V. Midha, Using metallic photonic crystals as visible light sources. *Phys. Rev. B* **86**, 174201 (2012)
4. O. Vazquez-Mena, T. Sannomiya, L.G. Villanueva, J. Voros, J. Brugger, Metallic nanodot arrays by stencil lithography for plasmonic biosensing applications. *ACS Nano* **5**, 844–853 (2011)
5. S. Chen, M. Svedendahl, T.J. Antosiewicz, M. Käll, Plasmon-enhanced enzyme-linked immunosorbent assay on large arrays of individual particles made by electron beam lithography. *ACS Nano* **7**, 8824–8832 (2013)
6. J. Wang, G. Duan, Y. Li, G. Liu, W. Cai, Wet etching-assisted colloidal lithography: a general strategy toward nanodisk and nanohole arrays on arbitrary substrates. *ACS Appl. Mater. Interfaces* **6**, 9207–9213 (2014)
7. A. Rajendran, M. Endo, Y. Katsuda, K. Hidaka, H. Sugiyama, Programmed two-dimensional self-assembly of multiple DNA origami jigsaw pieces. *ACS Nano* **5**, 665–671 (2011)
8. J.B. Edel, A.A. Kornyshev, M. Urbakh, Self-assembly of nanoparticle arrays for use as mirrors, sensors and antennas. *ACS Nano* **7**, 9526–9532 (2013)
9. Y. Zhong, Z. Wang, R. Zhang, F. Bai, H. Wu, R. Haddad, H. Fan, Interfacial self-assembly driven formation of hierarchically structured nanocrystals with photocatalytic activity. *ACS Nano* **8**, 827–833 (2014)
10. C.L. Nehl, H. Liao, J.H. Hafner, Optical properties of star-shaped gold nanoparticles. *Nano Lett.* **6**, 683–688 (2006)
11. S. Tokonami, Y. Yamamoto, H. Shiigi, T. Nagaoka, Synthesis and bioanalytical applications of specific-shaped metallic nanostructures: a review. *Anal. Chim. Acta* **716**, 76–91 (2012)
12. M.A. Mahmoud, M.A. El-Sayed, Different plasmon sensing behavior of silver and gold nanorods. *J. Phys. Chem. Lett.* **4**, 1541–1545 (2013)
13. T. Iida, Control of plasmonic superradiance in metallic nanoparticle assembly by light-induced force and fluctuations. *J. Phys. Chem. Lett.* **3**, 332–336 (2012)
14. S. Ito, H. Yamauchi, M. Tamura, S. Hidaka, H. Hattori, T. Hamada, K. Nishida, S. Tokonami, T. Itoh, H. Miyasaka, T. Iida, Selective optical assembly of highly uniform nanoparticles by doughnut-shaped beams. *Sci. Rep.* **3**, 3047 (2013)
15. M. Tamura, S. Ito, S. Tokonami, T. Iida, Theory for optical assembling of anisotropic nanoparticles by tailored light fields under thermal fluctuations. *Res. Chem. Intermed.* **40**, 2303–2313 (2014)
16. T. Iida, H. Ishihara, Theory of resonant radiation force exerted on nanostructures by optical excitation of their quantum states: from microscopic to macroscopic descriptions. *Phys. Rev. B* **77**, 245319 (2008)
17. T. Kim, K. Lee, M. Gong, S.-W. Joo, Control of gold nanoparticle aggregates by manipulation of interparticle interaction. *Langmuir* **21**, 9524–9528 (2005)
18. M. Tamura, T. Iida, Fluctuation-mediated optical screening of nanoparticles. *Nano Lett.* **12**, 5337–5341 (2012)
19. H.A. Atwater, A. Polman, Plasmonics for improved photovoltaic devices. *Nat. Mater.* **9**, 205–213 (2010)
20. K.G. Stamplecoskie, J.C. Scaiano, V.S. Tiwari, H. Anis, Optimal size of silver nanoparticles for surface-enhanced Raman spectroscopy. *J. Phys. Chem. C* **115**, 1403–1409 (2011)